Review of Scientific Instruments

Laboratory setup for extreme ultraviolet coherence tomography driven by a high-harmonic source

Cite as: Rev. Sci. Instrum. **90**, 113702 (2019); https://doi.org/10.1063/1.5102129
Submitted: 24 April 2019 • Accepted: 22 October 2019 • Published Online: 15 November 2019

Jan Nathanael, Martin Wünsche, Silvio Fuchs, et al.


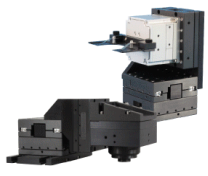
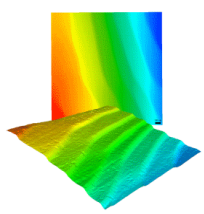
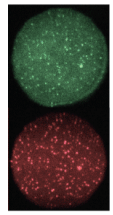

AIP Publishing

Review of Scientific Instruments ARTICLE scitation.org/journal/rsi

Laboratory setup for extreme ultraviolet coherence tomography driven by a high-harmonic source

Cite as: Rev. Sci. Instrum. 90, 113702 (2019); doi: 10.1063/1.5102129
Submitted: 24 April 2019 • Accepted: 22 October 2019 •
Published Online: 15 November 2019

Jan Nathanael,[1,2,a] Martin Wünsche,[1,2] Silvio Fuchs,[1,2] Thomas Weber,[1] Johann J. Abel,[1] Julius Reinhard,[1,2] Felix Wiesner,[1,2] Uwe Hübner,[3] Slawomir J. Skruszewicz,[1,2] Gerhard G. Paulus,[1,2] and Christian Rödel[1,2]

AFFILIATIONS

[1]Institute of Optics and Quantum Electronics, Friedrich Schiller University Jena, Max-Wien-Platz 1, 07743 Jena, Germany
[2]Helmholtz Institute Jena, Fröbelstieg 3, 07743 Jena, Germany
[3]Leibniz Institute of Photonic Technology, Albert-Einstein-Str. 9, 07745 Jena, Germany

[a)]jan.nathanael@uni-jena.de

ABSTRACT

We present a laboratory beamline dedicated to nanoscale subsurface imaging using extreme ultraviolet coherence tomography (XCT). In this setup, broad-bandwidth extreme ultraviolet (XUV) radiation is generated by a laser-driven high-harmonic source. The beamline is able to handle a spectral range of 30–130 eV and a beam divergence of 10 mrad (full width at half maximum). The XUV radiation is focused on the sample under investigation, and the broadband reflectivity is measured using an XUV spectrometer. For the given spectral window, the XCT beamline is particularly suited to investigate silicon-based nanostructured samples. Cross-sectional imaging of layered nanometer-scale samples can be routinely performed using the laboratory-scale XCT beamline. A depth resolution of 16 nm has been achieved using the spectral range of 36–98 eV which represents a 33% increase in resolution due to the broader spectral range compared to previous work.

I. INTRODUCTION

Silicon-based electronics have revolutionized our lives and societies in the past 50 years leading to, for example, integrated circuits which power consumer-grade electronics or specialized scientific and medical instruments. The density of transistors—the core elements of microchips—has increased rapidly over the last decades.[1,2] The structure size of semiconductor elements on a chip therefore shrunk from micrometers to the nanoscale. These nanostructures are typically produced for a mass market using optical projection lithography.[3,4] In this scheme, a photomask with the structural information is imaged on a silicon wafer using deep ultraviolet (DUV) light at about 193 nm. To increase the density of transistors further, nanostructures are stacked in layers.[5–7] Large efforts have been made in the last years to utilize extreme ultraviolet (XUV) radiation at 13.5 nm (also known as EUV) for further downsizing of silicon nanostructures to 7 nm.[8] The recent development of powerful EUV light sources with ~100 W has made EUV lithography economically attractive, and EUV lithography machines are currently being integrated into the production lines of computer chips worldwide.[8,9] For the nondestructive inspection of silicon-based nanoelectronics and lithography masks, imaging techniques with the nanometer resolution have to be developed—favorably using the same wavelengths which are used for the lithography process. Most of the commercially available imaging systems, e.g., for mask[10,11] or chip inspection,[12–14] are based on conventional imaging using DUV/EUV or x-ray light sources. In addition, *in situ* diagnostics for the layer thickness can become an important method for the fabrication process and quality control.

Driven by the development of powerful XUV and x-ray sources, cross-sectional imaging of silicon-based nanostructures such as integrated circuits became a very active field of research.[15–17] For most of these imaging techniques, large-scale synchrotron facilities and dedicated x-ray beamlines are commonly utilized. In recent years, laser-driven XUV sources with high spatial coherence have been developed that enable lensless imaging in laboratory setups with a

small footprint.[18–21] These XUV sources are typically based on the nonlinear conversion of femtosecond laser pulses in gaseous media by the process of high-harmonic generation (HHG).[22] For lensless imaging, where XUV sources with a small bandwidth are required, one harmonic is typically filtered by highly reflective multilayer mirrors.[23] Thus, most of the photon fluxes of broadband HHG sources are not exploited for imaging.

In contrast to monochromatic lensless imaging techniques, our approach exploits broad-bandwidth radiation by extending optical coherence tomography (OCT) into the XUV and the soft x-ray region,[24–27] hence the acronym extreme ultraviolet coherence tomography (XCT). We have developed this method for cross-sectional imaging of nanostructures. Using the spectral range of 36–98 eV, silicon-based nanostructures can be investigated. In this paper, we discuss the technical details of a dedicated XCT beamline that has been developed at the University of Jena. The XCT beamline allows measurements on a routine basis using computer-controlled beamline optics and online analysis software. In the XCT technique, subsurface imaging with the nanometer axial resolution is achieved by measuring the spectral reflectivity of the sample over a large bandwidth. Spectral modulations caused by spectral interference of reflections at interfaces in the sample are measured. The reflected spectrum is evaluated with an algorithm based on a Fourier transform to retrieve the depth profile of the nanostructure. XCT has repeatedly been demonstrated at synchrotron and lab-scale sources with axial resolutions in the order of a few nanometers.[27–30] Recently, we demonstrated 3D tomographic imaging of silicon-based nanostructures with an axial resolution of 24 nm using XCT and laser-driven XUV sources.[30] The lateral resolution is ~20 μm, which is currently limited by the XUV spot size on the sample surface.[30] This is sufficient to investigate, for example, test element group (TEG) patterns present in the scribe lines or so-called streets in the prediced state of semiconductor wafers in the manufacturing process.[31,32] Furthermore, XCT measurements provide a particularly sensitive material contrast—especially between lighter elements. For example, few-nanometer-thin silicon dioxide layers buried in silicon have been clearly detected using XCT. The existence of this layer was finally verified by transmission electron microscopy which, in contrast to XCT, required extensive preparation of the sample using focused ion beam milling and led to the destruction of the sample.[30]

II. TECHNICAL DETAILS OF THE XCT MICROSCOPE

The XCT beamline is located close to a high power femtosecond laser system in the laboratories of the Institute of Optics and Quantum Electronics. The femtosecond laser pulses are focused into the first vacuum chamber element of the XCT beamline. The main components of the XCT beamline are

1. an XUV source based on high-harmonic generation,
2. grazing incidence plates for separating XUV and laser radiation,
3. thin XUV transmissive metal filters to block the remaining laser radiation,
4. an XUV focusing unit,
5. a sample chamber with a positioning system, and
6. an XUV spectrometer and detector.

The entire apparatus, including an optical table for preparing and stabilizing the laser beam, measures ~4 m in length. A schematic of the XCT beamline is shown in Fig. 1. All flanges in the vacuum beamline are ConFlat type seals. For efficient differential pumping, copper plates with hole sizes corresponding to the XUV beam diameter are used between the vacuum elements.

A. XUV source

Broadband XUV radiation and soft x-rays can be generated by high-harmonic generation (HHG) from the interaction of femtosecond near-infrared laser pulses with gaseous media.[33–35]

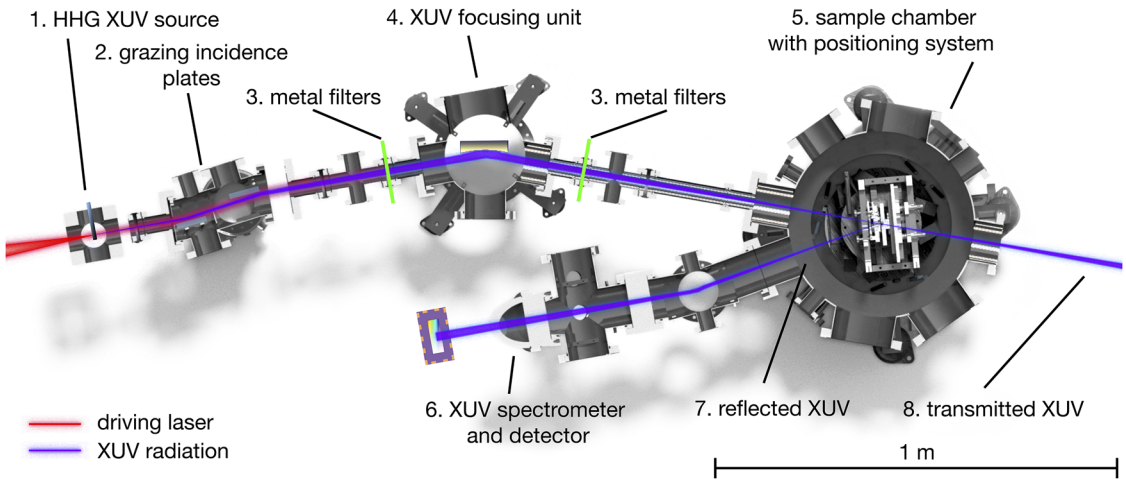

FIG. 1. Cross-sectional view of the XCT beamline with an (1) XUV source based on high-harmonic generation, (2) grazing incidence plates for separating the XUV and optical radiation, (3) XUV filter (green), (4) XUV focusing unit, (5) sample chamber with a positioning system, (6) XUV spectrometer and detector, and [(7) and (8)] reflected and transmitted XUV radiation.

HHG has the particular advantage that the radiation is spatially coherent.[35] The XUV beam has a low divergence such that the broadband radiation can be focused using, for example, a toroidal mirror in the grazing incidence geometry.[36] When laser pulses with a pulse duration of several cycles are used for HHG, an attosecond pulse train is created.[37] In the spectral domain, the attosecond pulse train corresponds to a comb of harmonics of the fundamental frequency. These intrinsic spectral modulations of HHG sources inhibit a straightforward use for XCT. Rather, a quasicontinuous spectrum is preferred for measuring the spectral reflectivity over the entire bandwidth. We therefore use femtosecond laser pulses from an optical parametric amplifier (OPA) whose central wavelength can be swept rapidly from 1260 nm to 1340 nm. Thus, a quasicontinuous spectrum is achieved according to the acquisition time of the detector.[38] The OPA is a commercial system (Light Conversion, UAB) with three nonlinear conversion stages. In order to pump the OPA, we use laser pulses with an energy of 9 mJ and a duration of 35 fs from a titanium sapphire femtosecond laser at a wavelength of 800 nm. The OPA pulses have a pulse duration of 55 fs and a repetition rate of 1 kHz. The system typically provides pulses with 2.4 mJ or an average power of 2.4 W at the signal wavelength of 1300 ± 40 nm. The laser pulses are then focused by a lens (f = 30 cm) into the interaction chamber shown in Fig. 1(1). High harmonics are generated by the nonlinear interaction of the femtosecond laser pulses with argon or neon gas. The gas is guided to the laser focus region inside the vacuum chamber using a nickel tube. Small holes are drilled into the nickel tube by the laser beforehand. The generated XUV radiation is emitted in the laser forward direction. This arrangement minimizes the gas load in the HHG interaction chamber while maintaining a relatively high gas density in the focal region and thus a high XUV yield. The HHG interaction chamber is pumped by using a 400 m^3/h Roots pump (Pfeiffer Vacuum GmbH). A backing pressure of about 500 mbar is applied for generating high harmonics in argon. This leads to a background gas pressure of about 5×10^{-2} mbar in the HHG interaction chamber. The harmonic emission was optimized using an XUV spectrometer that is calibrated in terms of the photon flux.[39] After filtering the near-infrared radiation with thin metal foils [Fig. 1(3)], the HHG source provides a photon flux of 4×10^9 photons/s for the spectral range of 30 eV–100 eV and 1×10^7 photons/s for the spectral range of 100 eV–200 eV.[38]

B. XUV filtering

The XUV radiation with a divergence of about 10 mrad copropagates with the near-infrared laser pulses to the next beamline section—a pair of coated substrates in grazing incidence [see Fig. 1(2)]. The grazing incidence plates have antireflective coatings for 1300 nm and are used to separate the reflected XUV radiation from the transmitted laser pulses. The top layer of the antireflective coating is a tantalum pentoxide layer that reflects the XUV radiation with a relatively high efficiency. In 7.5° grazing incidence geometry, this leads to a reflectivity of ~80% at 70 eV.[40] The combined XUV transmission of both grazing incidence plates in the spectral range of 30–130 eV is ~60%–40%.[40] At the same time, the power of the laser light is reduced to 10%, in this way avoiding damage to subsequent optical elements. With a water-cooled turbomolecular pump, a pressure of approx. 5×10^{-3} mbar is achieved in this beamline section. In the next beamline element shown in Fig. 1(3), thin metal foils (Lebow Company) are used as optical filters. The laser radiation is blocked (infrared transmission of ~10^{-4}) while the XUV radiation is transmitted. For the spectral range of 35–72 eV, ~250 nm aluminum filters with an XUV transmission of ~70%[40] are used. For the spectral range of 70–100 eV, ~200 nm zirconium filters with an XUV transmission of ~30%–50%[40] are applied. The metal filters are installed in the XUV beamline at two dedicated positions using customized gate valves (VAT group). This allows a quick change of the filter settings for the different spectral ranges. Since the metal foils are also gas-impermeable, they represent an efficient vacuum seal.

C. XUV focusing

In the focusing mirror unit shown in Fig. 1(4), a toroidal mirror is used for one-to-one imaging of the XUV source to the sample surface (optiX fab GmbH). The respective radii are 5757.5 mm and 173.6 mm. The mirror is coated with boron carbide which provides a reflectivity of 56%–85% for an incidence angle of 10° (30–130 eV bandwidth). Ray-tracing calculations using the ZEMAX software have shown that this focusing geometry is a good compromise between the XUV bandwidth, XUV divergence acceptance, and mirror size. The latter is 135 mm × 30 mm so that a solid angle of 23.5 mrad × 30 mrad (1.35° and 1.72°) is covered and the full HHG beam is focused. The focusing mirror can be aligned with a motorized 5D-stage (three axes of translation and tip-tilt) in order to minimize aberrations. The pressure in the focusing mirror section is ~5×10^{-7} mbar.

D. Sample chamber

The focused XUV beam is guided into the vacuum chamber shown in Fig. 1(5) where the samples are placed. A top view into the sample chamber is shown in Fig. 2. Ultrahigh vacuum (UHV) conditions of <10^{-8} mbar can be achieved, which reduces the formation of contamination layers on the sample surface (water, hydrocarbons, etc.). Indeed, we have observed XUV-induced formation

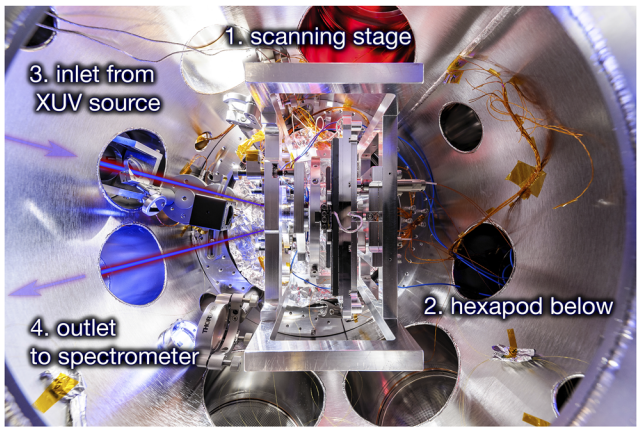

FIG. 2. Top view into the sample target chamber. The XUV radiation is focused onto the sample, which can be positioned with a hexapod system. The samples can be scanned laterally with high precision (1 nm) and a 100 mm travel range.

of carbon layers on the sample during our first XCT experiments where the vacuum pressure was only 10^{-5} mbar. The sample mount is supported by a hexapod system [Steward-platform type, Physik Instrumente (PI) GmbH & Co. KG]. The hexapod allows the sample mount to be positioned relative to the XUV beam in terms of X, Y, and Z with an accuracy of ~1 μm as well as tip, tilt, and rotation. In order to reduce the coupling of external vibrations, the hexapod is suspended in the chamber with coil springs and is magnetically damped. Further vibration isolation is accomplished using silicate rubber spacers between the hexapod and the sample mount. The sample mount is equipped with two translation stages (SmarAct GmbH, closed loop), which enable the positioning and fast lateral scans of samples with an accuracy of 1 nm and a repeatability of ±150 nm combined with a large travel distance of 103 mm. Samples with subsurface layer-type structures are typically manufactured on wafers with a diameter of 4 in. or less. The 2D scanning system allows the accurate positioning of such samples within an area of 103 mm × 103 mm relative to the XUV spot. Before each XCT measurement, the samples can be investigated in the visible range with an integrated long range optical microscope, whose spatial resolution is $\lesssim$1 μm. In addition, a scintillating screen (polished Ce:YAG crystal, 100 μm thickness, CRYTUR, spol. s r.o.) can be positioned in the sample plane to characterize the XUV focus. When performing XCT measurements, the angle of incidence to the normal of the sample is 15°(±1°).[30] The spectrometer is located at 30° to the incident beam so that the specularly reflected light is measured.

E. XUV spectrometer

The reflected XUV radiation is measured with a high-resolution and highly sensitive XUV spectrometer detector system. The spectrometer has a resolution of $\Delta E = 0.087$ eV over the spectral range of 30–70 eV. Details of the spectrometer can be found in Ref. 41. A large-area CCD camera is used as a detector (Andor Newton DO940P-BN, 2048 × 512 px, 13.5 μm pixel size).

III. XCT MEASUREMENTS USING THE LABORATORY MICROSCOPE

For XCT measurements, the spectral modulations that arise from the interference of the reflections at buried layers are recorded with the XUV spectrometer. Before we perform XCT measurements, we measure the reflected XUV spectrum from an inert material (titanium dioxide), which provides a reference spectrum for the entire XCT beamline. The spectral reflectivity of the sample is obtained by dividing the measured spectrum of the sample by the spectrum of the known inert material.

A. Data processing

In the following, we discuss the data processing of XCT measurements. The raw signal is obtained by a lineout of the camera image, which provides the counts C_i of every pixel i. Using a spectral calibration, every pixel i is linked to a wavelength λ_i, which provides the raw signal $C_i(\lambda_i)$. The reference signal $C_i^{\mathrm{Ref}}(\lambda_i)$ of the inert material is obtained in the same way. The reflectivity of the sample is then calculated by $R_i(\lambda_i) = R_i^{\mathrm{Ref}}(\lambda_i) \cdot C_i(\lambda_i)/C_i^{\mathrm{Ref}}(\lambda_i)$, where $R_i^{\mathrm{Ref}}(\lambda_i)$ is the known reflectivity of the inert material. This has the particular advantage that the sensitivity of the detector and the efficiency of the beamline components are not required to be known. In the next step, we transform $R_i(\lambda_i)$ into a k-space using the geometrical dispersion relation $\kappa_i = \frac{4\pi}{\lambda_i}\sqrt{n_D^2(\lambda_i) - \cos^2\vartheta}$. Here, n_D is the refractive index of the dominating material (Si in our case) and ϑ is the angle of incidence. It is important to note that κ_i is not equidistant. We perform a linear interpolation to resample the data set on an oversampled, equidistant, and zero padded grid. We further apply a Kaiser-Bessel function,

$$W(\kappa) = \begin{cases} \dfrac{I_0\left[\beta\sqrt{1-\left(\frac{2(\kappa-\gamma)}{\eta}\right)^2}\right]}{I_0(\beta)} & \text{for} \quad \kappa_{\min} \le \kappa \le \kappa_{\max}, \\ 0 & \text{else} \end{cases} \tag{1}$$

where I_0 is the modified Bessel function, $\eta = \kappa_{\max} - \kappa_{\min}$ and $\gamma = (\kappa_{\max} + \kappa_{\min})/2$ to the dataset Fourier artifacts are reduced. The Kaiser-Bessel window minimizes Fourier artifacts in the depth structure, in particular side-lobes, while the effective bandwidth and thus the resolution are reduced. A Fast Fourier Transform (FFT) of the filtered reflectivity yields an estimate of the axial structural information.[26,27] Since our scheme of XCT is based on common-path interferometry, spectral modulations are due to the optical path difference from the surface reflection to the layer reflection (cross-correlation terms) but also from the reflections between the layers themselves (autocorrelation terms). As a consequence, autocorrelation artifacts are present when the depth profile is evaluated using a simple Fourier transform of the spectral reflectivity.[30] These artifacts emerge in the XCT signal at depths, which correspond to the distance of two inner interfaces and thus do not represent a real interface at this position. To mitigate this ambiguity, a three-step phase retrieval (PR) algorithm has been developed which is described in the supplementary material of Fuchs *et al.*[30] In the PR-algorithm, the complex reflectivity

$$r(\kappa) = r_{\exp}(\kappa) \cdot e^{i\varphi(\kappa)} \tag{2}$$

is estimated using the measured spectrum $r_{\exp}(\kappa) = \sqrt{R_{\exp}(\kappa)}$ and a randomized phase $\varphi(\kappa)$ as an initial value. The algorithm uses a combination of a Gerchberg-Saxton[42] and a hybrid input-output[43] scheme to retrieve the unknown spectral phase. Finally, a Fourier transform of the complex reflectivity $r(\kappa)$, which includes the retrieved phase, yields the artifact-free depth structure. A schematic representation of the data processing steps of XCT is shown in Fig. 3.

B. High axial resolution XCT

The combination of two consecutive measurements in the spectral ranges of 36–72 eV (argon) and 72–98 eV (neon) for a sample with two buried gold layers (each 10 nm in thickness) at 220 nm and 335 nm is shown in Fig. 4(a). The usable bandwidth is mainly limited by the transmission window of the sample under investigation to 36–98 eV. The corresponding axial resolution considering a Kaiser-Bessel filter function with $\beta = 4$ is limited to approximately 16 nm. We want to note that the axial resolution defines the minimal distance of two neighboring interfaces that still appear separated from each other in the XCT signal (Rayleigh criterion). However, the precision of the absolute depth of an interface can be much

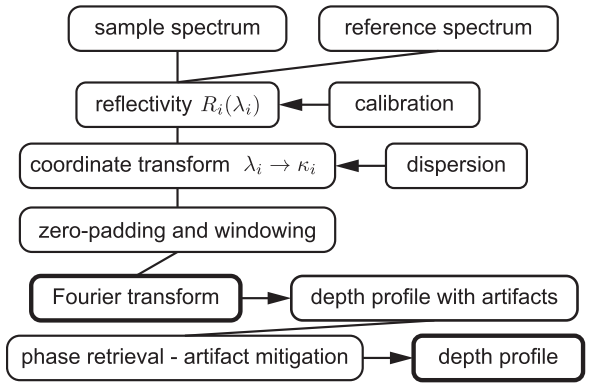

FIG. 3. Flow chart of the data processing to retrieve a XCT signal. The raw spectrum from the sample is divided by the raw spectrum of the reference material and yields the reflectivity $R_i(\lambda_i)$. The reflectivity is then transformed from wavelength to photon energy and wavenumber using the geometrical dispersion relation. The data are further linearly interpolated to an equidistant and zero-padded grid. A Fourier window is applied to mitigate side-lobe structures. A fast Fourier transform (FFT) and the phase retrieval algorithm are applied to yield the depth profile of the sample.

higher. Figure 4(b) shows the direct Fourier transform of the measured reflectivity depicted in Fig. 4(a). It can be seen that the XCT signal includes an autocorrelation artifact at ~111 nm, which corresponds to the distance of the two buried gold layers. After applying the PR-algorithm, the artifact is successfully eliminated as shown in the PR-XCT signal in Fig. 4(c). Both gold layers are clearly resolved. The retrieved depths, 220 ± 4 nm and 335 ± 4 nm, agree well with electron microscope measurements of the same sample.[30] According to the electron microscopy images of the sliced samples,[30] the thickness of the gold layers is ~10 nm. Consequently, the front and back sides of the layers cannot be resolved separately with the axial resolution of 16 nm. However, the layer thickness leads to prominent shoulders in the XCT signals. Two Gaussian curves are fitted to the peak at 220 nm in order to determine the location of the front side and the back side of the layer. The achieved axial resolution of the measurement is retrieved by evaluating the width (FWHM) of the Gaussian functions. The locations of the peaks of the Gaussian functions (220 nm and 233 nm) agree well with the locations of the front and back side interfaces of the layer in the sample (220 nm and 230 nm). The achieved axial resolution of 16 nm in XCT as well as PR-XCT matches the anticipated resolution from the theory precisely. The broader appearance of the peak at 335 nm in the XCT signal and 333 nm in the PR-XCT signal results from laser fluctuations. These time dependent fluctuations cause small deviations between the source spectrum of the reference measurement and the source spectrum of the actual measurement. This leads to residual harmonic oscillations in the measured reflectivity. The high-order harmonics are modulated with twice the driving laser frequency. At driving wavelengths of 1260 nm–1340 nm, the residual harmonic modulation frequency corresponds to a depth of ~325 nm in the XCT signal and thus overlaps with the lower gold layer.

We typically have acquisition times between 5–60 s in the spectral range of 35–72 eV. This is remarkable since the reflectivity on near-normal incidence is of the order of only 10^{-3}. Exposure

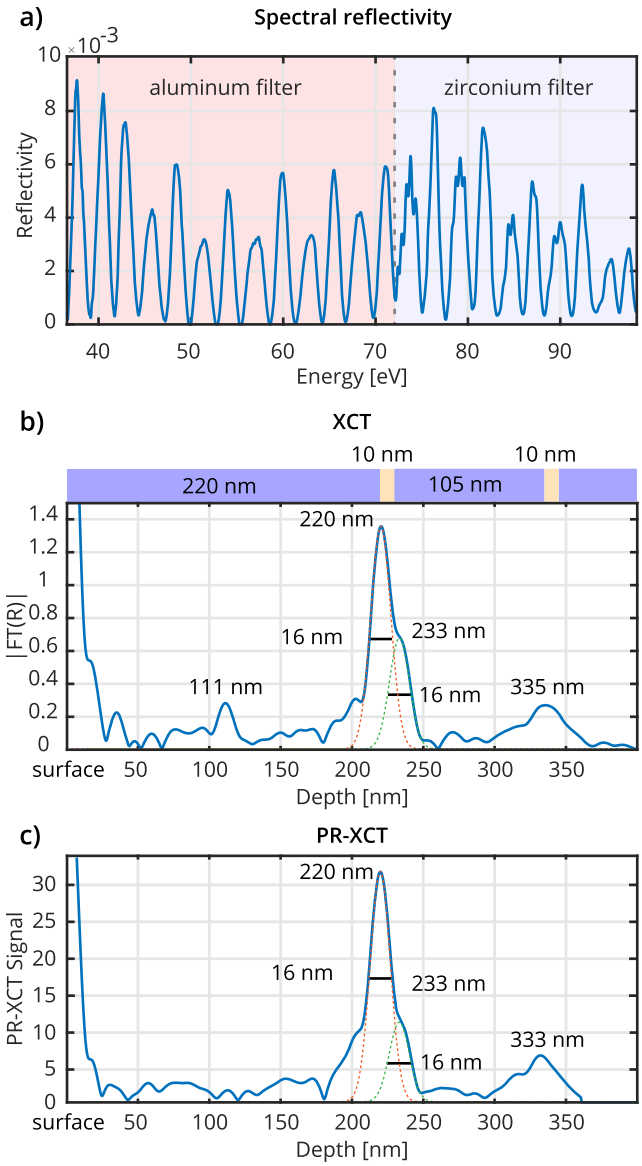

FIG. 4. The spectral XUV reflectivity recorded with the XCT beamline and its retrieved depth structure. (a) The spectral reflectivity from a nanostructured layered sample shows characteristic modulations which are due to spectral interference. The spectral region highlighted in red is 36–72 eV and in blue is 72–98 eV, corresponding to measurements with different filter settings. (b) The depth profile of the sample is reconstructed from the spectral reflectivity using a Fourier-transform. Peaks are located at 220 ± 4 nm and 335 ± 4 nm with an axial resolution of 16 nm. Two Gaussian curves are fitted to the peak at 220 nm in order to determine the location of the front and back sides of the layer and to retrieve the achieved axial resolution of the measurement by evaluating the width (FWHM) of the Gaussian functions. As a guide to the eye, a schematic of the sample shows the depths of each layer. It can be seen that the XCT signal includes an autocorrelation artifact at ~111 nm, which corresponds to the distance of the two buried gold layers.[30] (c) Depth structure after applying the phase retrieval algorithm. Peaks are located at 220 ± 4 nm and 333 ± 4 nm. The axial resolution remains the same at 16 nm. The autocorrelation artifact at ~111 nm is eliminated.

times in the spectral range of 72–98 eV are usually a few minutes. After the acquisition, the reconstruction of the depth profile can be immediately computed. The computation times, even including the PR-algorithm, are usually much shorter than the acquisition times. Therefore, an online reconstruction is possible and helpful to find the area on the sample which can be investigated with a lateral scan.

C. Lateral XCT scan

We have performed three-dimensional measurements restricted to the aluminum window spectral range (41–72 eV) at a lateral sampling with a step size of 90 μm; see Fig. 5. While compromising in the axial resolution, the limited spectral range with shorter exposure times per point allows for a much shorter overall scanning time. The raw dataset contains 3569 individual measurement points, which was recorded within ~11 h.

Three-dimensional cross-sectional images of a sample containing two laterally structured buried thin gold layers are shown in Fig. 5 using the Fourier transform and the PR-algorithm for the reconstruction of the depth profile. For each lateral point, the spectral phases are retrieved independently from neighboring points, which indicates the robustness of the algorithm. For PR-XCT, the artifacts are strongly suppressed. Using a spectral range from 41 nm to 72 eV, a resolution of 38 nm (Kaiser-Bessel function $\beta = 6$) in the axial direction has been obtained. The measurement was optimized to minimize the acquisition time. Therefore, only aluminum filters have been used limiting the spectral range to 72 eV. On the other hand, we compromised between the acquisition time and noise at the low photon energy side of the spectrum, limiting the spectral window to a beginning of 41 eV. Two buried gold layers were measured in a depth of 227 ± 4 nm and 333 ± 4 nm, respectively. In addition, a silicon dioxide layer could be identified in a depth of 161 ± 4 nm due to the high contrast of the complex refractive indices of silicon and oxygen in the XUV. Interestingly, electron microscopy can hardly resolve this layer due to the relatively small density difference of silicon and silicon dioxide.[30]

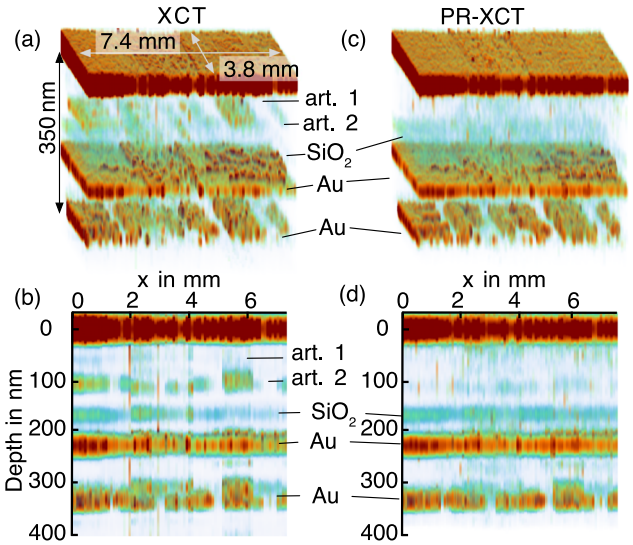

FIG. 5. A 3D cross-sectional image is shown that has been recorded with the subsurface imaging technique XCT. Two buried gold layers and a silicon oxide layer have been revealed with an axial resolution of 38 nm. In [(a) and (b)], plain XCT results are shown, whereas in [(c) and (d)] phase-retrieval XCT results are presented to highlight the potential of artifact mitigation. The same dataset was used. It is worth noting the absence of artifacts in [(c) and (d)] in comparison to [(a) and (b)] where art. 1 and art. 2 are present. For the shown XCT measurements, the XUV spot size is 90 μm × 80 μm.

IV. CONCLUSION AND OUTLOOK

XCT is a powerful subsurface imaging technique which facilitates noninvasive 3D cross-sectional imaging. We have presented the technical details of a laboratory-scale beamline that allows XCT measurements of silicon-based nanostructures on a routine basis. An axial resolution of 16 nm, which is mainly limited by the utilized XUV bandwidth, has been demonstrated. Data acquisition and analysis tools as well as automated lateral scans have been integrated in the XCT beamline, which allows XCT measurements of layered nanostructures to be performed in a routinely and consistent manner. The XCT beamline enables the inspection and measurements of silicon-based nanostructures. For example, typically used test structures in the lithographic process (e.g., scribe line TEG patterns[31,32]) can be investigated with the XCT technique. XCT has the potential to become a diagnostics tool in the inspection of layered nanostructures which are relevant for the semiconductor industry. Due to the high element-specific contrast of the complex refractive index in the XUV, impurities can be measured with high sensitivity. This may enable the use of XCT in the quality control of thin films and the noninvasive investigation of buried layers of 2D materials such as graphene or transition metal dichalcogenides.[44]

ACKNOWLEDGMENTS

The authors acknowledge funding by the Deutsche Forschungsgemeinschaft (DFG) (Grant Nos. PA 730/5 and 381425468), Bundesministerium für Bildung und Forschung (BMBF) (VIP "X-CoherenT"), and Thüringer Aufbaubank (TAB) (Grant Nos. 2015FGR0094 and 2018FGR0080). Christian Rödel acknowledges support from the Volkswagen Foundation.

REFERENCES

[1] M. Neisser and S. Wurm, Adv. Opt. Technol. **1**, 217 (2012).
[2] S. Okazaki, Microelectron. Eng. **133**, 23 (2015).
[3] R. Menon, A. Patel, D. Gil, and H. I. Smith, Mater. Today **8**, 26 (2005).
[4] S. Owa and H. Nagasaka, J. Micro/Nanolithogr., MEMS, MOEMS **3**, 97 (2004).
[5] R. Shirota, in *Advances in Non-Volatile Memory and Storage Technology*, edited by Y. Nishi (Woodhead Publishing, 2014), pp. 27–74.
[6] C. M. Compagnoni, A. Goda, A. S. Spinelli, P. Feeley, A. L. Lacaita, and A. Visconti, Proc. IEEE **105**, 1609 (2017).
[7] A. Goda and K. Parat, in *2012 International Electron Devices Meeting, 10–13 December 2012, San Francisco, CA, USA* (IEEE, 2012), p. 2.1.1.
[8] M. Green, Y. Choi, Y. Ham, H. Kamberian, C. Progler, S.-E. Tseng, T.-B. Chiou, J. Miyazaki, A. Lammers, and A. Chen, Proc. SPIE **10450**, 1045005 (2017).
[9] H. Mizoguchi, H. Nakarai, T. Abe, K. M. Nowak, Y. Kawasuji, H. Tanaka, Y. Watanabe, T. Hori, T. Kodama, Y. Shiraishi *et al.*, in *Semiconductor Technology International Conference (CSTIC), 2018* (IEEE, China, 2018), pp. 1–7.
[10] R. Capelli, D. Hellweg, M. Dietzel, M. Koch, C. Wolke, and G. Kersteen, Proc. SPIE **10583**, 1058311 (2018).

[11]D. Hellweg, J. Ruoff, A. Herkommer, J. Stühler, T. Ihl, H. Feldmann, M. Ringel, U. Strößner, S. Perlitz, and W. Harnisch, Proc. SPIE **7969**, 79690H (2011).
[12]W. Chao, B. D. Harteneck, J. A. Liddle, E. H. Anderson, and D. T. Attwood, Nature **435**, 1210 (2005).
[13]H. Huang, S. A. Eddinger, and M. Schoff, Fusion Sci. Technol. **55**, 373 (2009).
[14]C. Schmidt, S. T. Kelly, Y. Wang, S. Coyle, and M. H. Shearer, in *2017 IEEE 24th International Symposium on the Physical and Failure Analysis of Integrated Circuits (IPFA)* (IEEE, 2017), pp. 1–4.
[15]J. Deng, Y. P. Hong, S. Chen, Y. S. G. Nashed, T. Peterka, A. J. F. Levi, J. Damoulakis, S. Saha, T. Eiles, and C. Jacobsen, Phys. Rev. B **95**, 104111 (2017).
[16]Y.-S. Yu, M. Farmand, C. Kim, Y. Liu, C. P. Grey, F. C. Strobridge, T. Tyliszczak, R. Celestre, P. Denes, J. Joseph, H. Krishnan, F. R. N. C. Maia, A. L. D. Kilcoyne, S. Marchesini, T. P. C. Leite, T. Warwick, H. Padmore, J. Cabana, and D. A. Shapiro, Nat. Commun. **9**, 921 (2018).
[17]M. Holler, M. Guizar-Sicairos, E. H. R. Tsai, R. Dinapoli, E. Müller, O. Bunk, J. Raabe, and G. Aeppli, Nature **543**, 402 (2017).
[18]R. L. Sandberg, A. Paul, D. A. Raymondson, S. Hädrich, D. M. Gaudiosi, J. Holtsnider, R. I. Tobey, O. Cohen, M. M. Murnane, H. C. Kapteyn, C. Song, J. Miao, Y. Liu, and F. Salmassi, Phys. Rev. Lett. **99**, 098103 (2007).
[19]M. D. Seaberg, B. Zhang, D. F. Gardner, E. R. Shanblatt, M. M. Murnane, H. C. Kapteyn, and D. E. Adams, Optica **1**, 39 (2014).
[20]M. Zürch, J. Rothhardt, S. Hädrich, S. Demmler, M. Krebs, J. Limpert, A. Tünnermann, A. Guggenmos, U. Kleineberg, and C. Spielmann, Sci. Rep. **4**, 7356 (2014).
[21]G. Tadesse, W. Eschen, R. Klas, V. Hilbert, D. Schelle, A. Nathanael, M. Zilk, M. Steinert, F. Schrempel, T. Pertsch *et al.*, Sci. Rep. **8**, 8677 (2018).
[22]M. Ferray, A. L'Huillier, X. F. Li, L. A. Lompre, G. Mainfray, and C. Manus, J. Phys. B: At., Mol. Opt. Phys. **21**, L31 (1988).
[23]S. A. Yulin, T. Kuhlmann, T. Feigl, and N. Kaiser, Proc. SPIE **5037**, 286 (2003).
[24]G. G. Paulus and C. Rödel, U.S. Patent 7656538 (2 February 2010).
[25]S. De Rossi, D. Joyeux, P. Chavel, N. De Oliveira, M. Richard, C. Constancias, and J.-Y. Robic, Appl. Opt. **47**, 2109 (2008).
[26]S. Fuchs, A. Blinne, C. Rödel, U. Zastrau, V. Hilbert, M. Wünsche, J. Bierbach, E. Frumker, E. Förster, and G. G. Paulus, Appl. Phys. B **106**, 789 (2012).
[27]S. Fuchs, C. Rödel, A. Blinne, U. Zastrau, M. Wünsche, V. Hilbert, L. Glaser, J. Viefhaus, E. Frumker, P. Corkum, E. Förster, and G. G. Paulus, Sci. Rep. **6**, 20658 (2016).
[28]P. Wachulak, A. Bartnik, and H. Fiedorowicz, Sci. Rep. **8**, 8494 (2018).
[29]Y.-Y. Li, Y.-W. Lee, T.-S. Ho, J.-H. Wang, I.-C. Wu, T.-W. Hsu, Y.-T. Chen, and S.-L. Huang, Opt. Lett. **43**, 4029 (2018).
[30]S. Fuchs, M. Wünsche, J. Nathanael, J. J. Abel, C. Rödel, J. Biedermann, J. Reinhard, U. Hübner, and G. G. Paulus, Optica **4**, 903 (2017).
[31]B.-T. Jang and K.-H. Kim, U.S. Patent 6707064 (16 March 2004).
[32]J. Ellis, U.S. Patent 7303844 (4 December 2007).
[33]E. Constant, D. Garzella, P. Breger, E. Mével, C. Dorrer, C. Le Blanc, F. Salin, and P. Agostini, Phys. Rev. Lett. **82**, 1668 (1999).
[34]A. Rundquist, Z. Chang, H. Wang, I. Christov, H. C. Kapteyn, and M. M. Murnane, AIP Conf. Proc. **426**, 296 (1998).
[35]T. Popmintchev, M.-C. Chen, D. Popmintchev, P. Arpin, S. Brown, S. Ališauskas, G. Andriukaitis, T. Balčiunas, O. D. Mücke, A. Pugzlys, A. Baltuška, B. Shim, S. E. Schrauth, A. Gaeta, C. Hernández-García, L. Plaja, A. Becker, A. Jaron-Becker, M. M. Murnane, and H. C. Kapteyn, Science **336**, 1287 (2012).
[36]H. Mashiko, A. Suda, and K. Midorikawa, Appl. Opt. **45**, 573 (2006).
[37]P. Antoine, A. L'Huillier, and M. Lewenstein, Phys. Rev. Lett. **77**, 1234 (1996).
[38]M. Wünsche, S. Fuchs, S. Aull, J. Nathanael, M. Möller, C. Rödel, and G. G. Paulus, Opt. Express **25**, 6936 (2017).
[39]S. Fuchs, C. Rödel, M. Krebs, S. Hädrich, J. Bierbach, A. E. Paz, S. Kuschel, M. Wünsche, V. Hilbert, U. Zastrau, E. Förster, J. Limpert, and G. G. Paulus, Rev. Sci. Instrum. **84**, 023101 (2013).
[40]B. Henke, E. Gullikson, and J. Davis, At. Data Nucl. Data Tables **54**, 181 (1993).
[41]M. Wünsche, S. Fuchs, T. Weber, J. Nathanael, J. J. Abel, J. Reinhard, F. Wiesner, U. Hübner, S. J. Skruszewicz, G. G. Paulus *et al.*, Rev. Sci. Instrum. **90**, 023108 (2019).
[42]R. Gerchberg and W. Saxton, Optik **35**, 227 (1972).
[43]J. R. Fienup, Opt. Lett. **3**, 27 (1978).
[44]Q. H. Wang, K. Kalantar-Zadeh, A. Kis, J. N. Coleman, and M. S. Strano, Nat. Nanotechnol. **7**, 699 (2012).